Water wave scattering by a structured ridge on the sea bed

R. Porter* and C. Marangos

School of Mathematics, Fry Building, Woodland Road, University of Bristol, Bristol, BS8 1UG, UK.

Abstract

The propagation of plane incident waves over a long submerged uniform rectangular structured ridge protruding from the sea bed is considered. The ridge is comprised of a uniform closely-spaced array of vertical barriers between which the fluid is allowed to flow. In addition to the height and width of the ridge, the orientation and thickness of the barriers are adjustable design parameters. Particular interest centres on the ability of the ridge to negatively refract obliquely-incident waves and this is shown to be possible provided the barriers extend sufficiently close to the surface. A key result is that the modulus of reflection and transmission coefficients are symmetric functions of the incident wave heading and the barrier orientation. This implies perfect transmission of wave energy for thin barrier elements at incident angles that are the reverse of the barrier orientation, extending the result of Porter (2021) to structured plate arrays of any submergence. The paper details two mathematical approaches to the solution of the problem, one for general barrier orientations and the other for a specific orientation where special treatment of the resulting problem is required. Numerical computations compare favourably with a variety of established results and good agreement with an existing shallow water approximation is confirmed for sufficiently long wavelengths.

Keywords: Water waves, metamaterials, bathymetry, negative refraction.

1 Introduction

The bespoke manipulation of water waves by rigid bathymetric structures immersed in a fluid with a free surface has been the main subject of interest in a number of recent papers: see, for e.g., Farhat *et al.* (2008), Chen *et al.* (2009), Farhat *et al.* (2010), Berraquero *et al.* (2013), Maurel *et al.* (2017), Maurel *et al.* (2019), Marangos & Porter (2021), Porter *et al.* (2021).

These studies have been principally motivated by the application of so-called metamaterials to problems relating to electromagnetic, acoustic and elastic wave propagation in which devices are created to manipulate waves in ways that are inaccessible using conventional materials (an extensive modern catalogue of examples is described in collection of volumes edited by Maier (2018)). A metamaterial is typically defined by elements forming a microstructure possessing a lengthscale that is significantly smaller than the underlying wavelength and designed to produce unusual macroscopic effects on the wavefield. In water waves this includes, for example, negative gravity (e.g. Hu *et al.* (2013)) and negative refraction (e.g. Farhat *et al.* (2010), Marangos & Porter (2021)).

*Corresponding author (richard.porter@bristol.ac.uk)

The earliest application of metamaterials in a water waves setting was described by Farhat *et al.* (2008) who considered an annular ring device comprised of closely-spaced vertical posts extending uniformly through the fluid as an invisibility cloak, designed to bend incoming waves entering the device around the centre of the ring without distorting the wavefield outside the ring. Berraquero *et al.* (2013) used a closely-spaced array of submerged rectangular ridges protruding upwards from the bottom as a device for perfectly transmitting waves through a sharp bend in a channel of uniform width. In both these contributions the exact governing equations are reduced to approximate two-dimensional equations, independent of the depth, involving a rank-2 tensor whose elements encode the macroscale influence of the microstructure through homogenisation. This independent spatial control of two perpendicular components of the wave speed is now influenced by the design of elements of the microstructure. In certain applications such as cloaking (e.g. Farhat *et al.* (2008), Zareei & Alam (2015)), a coordinate transformation method prescribes this design.

The analysis for Berraquero *et al.* (2013) was performed under so-called shallow water theory which, as the name suggests, is an approximation which applies when the depth of the fluid is small compared to both the wavelength and horizontal lengthscales over which significant changes depth occur. Their homogenisation, which did not to take into account this latter restriction, was later improved upon by Maurel *et al.* (2017) whilst effective matching conditions on boundaries of the water wave metamaterial were established in Maurel *et al.* (2019) allowing them to consider the topic of the present study: plane wave scattering by a long structured ridge of finite width. All three contributions mentioned above were performed under the restriction of shallow water theory. Marangos & Porter (2021) also developed a shallow water model which complements those earlier models by assuming the gaps between the rectangular protrusions in the bed are small relative to their height. Whilst the model of Maurel *et al.* (2017) relied upon (albeit simple) computations of the effective depths, in the method of Marangos & Porter (2021) these expressions were explicit.

The same close-spacing assumption has recently been used in Porter *et al.* (2021) to consider scattering of wave by a vertical plate array structure confined within a truncated cylinder protruding from the bottom of the fluid. In that work, the results from the shallow water theory of Marangos & Porter (2021) was compared with a full depth-dependent treatment of the problem. As expected, the agreement between exact and approximate theories was shown to be good provided the depth to wavelength ratio was sufficiently small.

Significantly, the work of Porter *et al.* (2021) was the first to consider a bathymetric water wave microstructure under full depth-dependent theory and the solution posed mathematical challenges. In particular, in seeking separation solutions in the domain including the structured bed, it becomes necessary to determine the eigenvalues of a non-trivial dispersion relation. The present paper is closely related to Porter *et al.* (2021) but here we consider plane wave scattering by a long submerged uniform rectangular ridge formed by a plate array. This is geometrically simpler than the truncated cylinder of Porter *et al.* (2021). In particular, the factorisation of the longshore wavenumber dependence from the problem results in a two-dimensional problem in a vertical cross section perpendicular to the longshore direction. In seeking eigensolutions over the structured bed a non-trivial dispersion relation results. However, apart from special cases, it is found that eigenvalues lie in the complex plane and this brings an added complication to the mathematical and numerical solutions not encountered in Porter *et al.* (2021).

In addition to the developing solutions to the general problem we will be interested in comparing solutions to the shallow water approximation of Marangos & Porter (2021) and to other special cases. These include the case where the barriers forming the structured ridge are aligned with the longshore direction, a consequence of which matching conditions along the lateral edges of the ridge change character. We take advantage of this to develop a new approach (this appears in Section

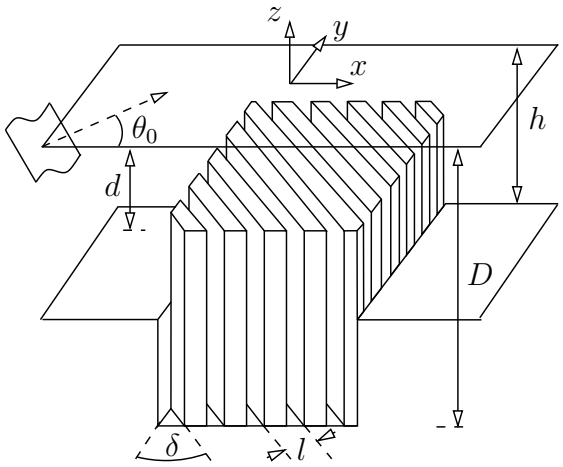

Figure 1: The most general configuration of the structured ridge of width $2b$.

3) which is based on the formulation and solution of integral equations, similar to Porter & Evans (1995), This approach makes it simpler to consider a fluid depth within the structured array which is different to the fluid depth away from the ridge. This contrasts with the eigenfunction matching method used for the general orientation of the barriers developed in Section 2 which is most easily applied in the case where the total fluid depths inside and outside the ridge are the same. In Section 4, we discuss numerical methods and convergence to existing results. Of particular interest will be the influence of the depth of submergence of the top of the ridge below the surface and the effect this has on its refractive properties.

2 Formulation and solution

Cartesian coordinates (x, y, z) are used with z directed vertically upwards from an origin lying in the mean free surface of the fluid. In the semi-infinite regions $x < -b$ and $x > b$ the fluid is of uniform constant depth h. In the strip $-b < x < b$ a closely-spaced periodic array of vertical barriers of width $l\Theta$ protrude upwards from a constant depth D to a depth d below the surface. The narrow gaps between the barriers are of width $(1-\Theta)l$ and the barriers are rotated through an anticlockwise angle δ with respect to the (x, z) plane. See Fig. 1. The geometry is therefore specified in exactly the same way as, and with almost identical notation to, Marangos & Porter (2021).

A plane wave is incident from $x = -\infty$ and propagates at an anticlockwise angle $\theta_0 \in (-\pi/2, \pi/2)$ with respect to the positive x-direction. The wave is partially reflected and partially transmitted with amplitudes described by reflection and transmission coefficients R and T, being the principal unknowns in the problem.

Working within the assumptions of classical linearised theory, namely that the fluid is inviscid and incompressible and its motion assumed to be irrotational and of small amplitude, there exists a velocity potential $\phi(x, y, z)$ relating to motion of a single radian frequency ω that satisfies

$$\nabla^2\phi = 0, \qquad \text{in the fluid} \tag{1}$$

and

$$\phi_z - K\phi = 0, \qquad \text{on } z = 0 \tag{2}$$

where $K=\omega^2/g$ with

$$\hat{\mathbf{n}}\cdot\nabla\phi=0 \tag{3}$$

on all rigid submerged boundaries having unit outward normal $\hat{\mathbf{n}}$. In $x<-b$ and $x>b$ (3) reduces to $\phi_z=0$ on $z=-h$ and we have

$$\phi(x,y,z)\sim\begin{cases}(\mathrm{e}^{\mathrm{i}\alpha_0 x}+R\mathrm{e}^{-\mathrm{i}\alpha_0 x})\mathrm{e}^{\mathrm{i}\beta_0 y}\psi_0(z), & x\to-\infty\\ T\mathrm{e}^{\mathrm{i}\alpha_0 x}\mathrm{e}^{\mathrm{i}\beta_0 y}\psi_0(z), & x\to\infty\end{cases} \tag{4}$$

where $\alpha_0=k\cos\theta_0$, $\beta_0=k\sin\theta_0$. Here

$$\psi_0(z)=N_0^{-1/2}\cosh k(z+h),\qquad N_0=\frac{1}{2}\left(1+\frac{\sinh 2kh}{2kh}\right) \tag{5}$$

and k is the real positive root of $K=k\tanh kh$.

Within $|x|<b$ and $-d<z<0$, above the structured plate array, (1) continues to hold. For $|x|<b$ and $-D<z<-d$ we can approximate the effect of the interaction of the fluid and the vertical barriers by introducing an effective medium equation (as in Porter (2021), Marangos & Porter (2021), Zheng *et al.* (2021)) given by

$$\Phi_{YY}+\Phi_{zz}=0 \tag{6}$$

for $\phi(x,y,z)\equiv\Phi(X,Y,z)$ where (X,Y) are coordinates rotated through an angle δ from (x,y) via the transformation

$$\begin{pmatrix}X\\Y\end{pmatrix}=\mathcal{R}\begin{pmatrix}x\\y\end{pmatrix},\quad\text{where}\quad\mathcal{R}=\begin{pmatrix}\cos\delta&\sin\delta\\-\sin\delta&\cos\delta\end{pmatrix}. \tag{7}$$

The governing equation (6) is derived by exploiting a contrast in lengthscales between the narrow gaps between the barriers and other lengthscales in the problem. That is, we require l to be significantly smaller than $D-d$, b, $1/k$, all of which are regarded as being of similar orders magnitude. Then the ratio of $l/(D-d)$, say, forms a small parameter, ϵ, say, which is used to develop the approximation (6) through a standard multiple-scales approach – see Porter (2021) for details. In addition

$$\Phi_z=0,\qquad\text{on } z=-D \tag{8}$$

holds and, at boundaries between the structured plate array and the surrounding fluid, effective conditions can be derived at leading order in ϵ which require the local matching of pressures and fluxes across those boundaries. For $|x|<b$ this is expressed as

$$\Phi|_{-d^-}=\phi|_{-d^+}\qquad\text{and}\qquad(1-\Theta)\Phi_z|_{-d^-}=\phi_z|_{-d^+}. \tag{9}$$

We will specify conditions that hold on the lateral boundaries, $x=\pm b$, later.

For now, we remark that replacing the detailed flow within and into the microstructure by a flow governed by effective equations and boundary conditions implies a geometric invariance in the y coordinate and this implies that the solution everywhere inherits the y-variation of the incident wave. In other words we can write

$$\phi(x,y,z)=\varphi(x,z)\mathrm{e}^{\mathrm{i}\beta_0 y} \tag{10}$$

everywhere, including within the region $|x| < b$, $-D < z < -d$ governed by (6) in transformed coordinates. Now we can write the full solution in $x < -b$ as

$$\varphi(x,y) = (\mathrm{e}^{\mathrm{i}\alpha_0 x} + R\mathrm{e}^{-\mathrm{i}\alpha_0 x})\psi_0(z) + \sum_{n=1}^{\infty} a_n \mathrm{e}^{\alpha_n(x+b)}\psi_n(z) \tag{11}$$

and in $x > b$ as

$$\varphi(x,y) = T\mathrm{e}^{\mathrm{i}\alpha_0 x}\psi_0(z) + \sum_{n=1}^{\infty} b_n \mathrm{e}^{-\alpha_n(x-b)}\psi_n(z) \tag{12}$$

in which a_n, b_n are expansion coefficients, $\alpha_n = (\beta_0^2 + k_n^2)^{1/2}$ and

$$\psi_n(z) = N_n^{-1/2}\cos k_n(z+h), \qquad N_n = \frac{1}{2}\left(1 + \frac{\sin 2k_n h}{2k_n h}\right). \tag{13}$$

Here, k_n are the increasing sequence of positive roots of $K = -k_n \tan k_n h$ for $n \geq 1$. Writing $k_0 = -\mathrm{i}k$ extends this definition to include the propagating wavenumber. Then it is known that the depth eigenfunctions are orthogonal, satisfying

$$\int_{-h}^{0} \psi_n(z)\psi_m(z)\,dz = h\delta_{m,n}, \qquad \text{for } m,n \geq 0. \tag{14}$$

Within $|x| < b$ we use (7) to write (6)

$$\phi_{zz} + \left(-\sin\delta\frac{\partial}{\partial x} + \cos\delta\frac{\partial}{\partial y}\right)^2 \phi = 0 \tag{15}$$

and then, using (10), reduce this equation, which holds over $-D < z < -d$, to

$$\varphi_{zz} + \left(-\sin\delta\frac{\partial}{\partial x} + \mathrm{i}\beta_0\cos\delta\right)^2 \varphi = 0. \tag{16}$$

Likewise, the governing equation (1) in $-d < z < 0$ is reduced using (10) to

$$\varphi_{zz} + \varphi_{xx} - \beta_0^2\varphi = 0 \tag{17}$$

and these two equations govern in contiguous domains upon whose horizontal boundaries the conditions $\varphi_z - K\varphi = 0$ on $z = 0$, $\varphi_z = 0$ on $z = -D$ apply in addition to matching conditions: φ is continuous across $z = -d$ and $\varphi_z(x, -d^+) = (1-\Theta)\varphi_z(x, -d^-)$.

In seeking solutions of the form $\varphi(x,z) = \mathrm{e}^{\mathrm{i}\mu x}Z(z)$ we find that

$$Z(z) = \begin{cases} \cosh\lambda z + (K/\lambda)\sinh\lambda z, & -d < z < 0 \\ A(\mu)\cosh\kappa(z+D), & -D < z < -d \end{cases} \tag{18}$$

(defined such that $Z(0) = 1$) where

$$A(\mu) = \frac{\cosh\lambda d - (K/\lambda)\sinh\lambda d}{\cosh\kappa(D-d)} \tag{19}$$

and

$$\lambda^2 = \mu^2 + \beta_0^2, \qquad \kappa = \mu\sin\delta - \beta_0\cos\delta \tag{20}$$

satisfy the dispersion relation

$$(1-\Theta)\kappa\tanh(\kappa(D-d)) = \lambda\frac{K-\lambda\tanh\lambda d}{\lambda - K\tanh\lambda d}. \tag{21}$$

For general parameters the roots of this dispersion relation are complex and the task of locating roots is typically not easy. We note that if μ is a root then so is $\bar{\mu}$, its complex conjugate, but $-\mu$ is not a root unless $\Theta = 1$, $D = d$, $\beta_0 = 0$ or $\delta = 0, \pi/2$. For these parameter sets all roots can be shown to lie either on the real or imaginary μ-axes and we can use any of these cases as the basis for a numerical scheme which track roots as the parameters change. In particular when $\beta_0 = 0$, corresponding to normal wave incidence, $\theta_0 = 0$, (21) reduces to

$$(1-\Theta)\sin\delta\tanh(\mu(D-d)\sin\delta) = \frac{K-\mu\tanh\mu d}{\mu - K\tanh\mu d} \tag{22}$$

and it is shown in Porter *et al.* (2021) (this can be mapped to their relation using $(1-\Theta)\sin\delta = \cos t$ and $(D-d)\sin\delta = (h-d)\cos t$ to define an equivalent t and h) that this equation has two real roots $\mu = \pm\mu_0$ and an infinite sequence of roots $\mu = \pm\mu_n$, $n = 1, 2, \ldots$ lying on the imaginary axis. In Porter *et al.* (2021) it was shown how to locate all these roots and, crucially, it was proved that no roots lie away from the real or imaginary axes in the complex plane.

Assuming that roots of (22) have been determined and that roots vary continuously as a function of β_0 we we can increase β_0 in small steps to the value required allowing us to numerically track the new location of roots in the complex plane as each step is made. Practically, this is done using Newton iteration. In most cases with steps of 1 degrees and 20 iterations at each step are sufficient to reach solutions of (21) accurate to 12 decimal places. However, there are some cases where computations require increased refinement, especially when Θ is not small or when kh is large and when we seek roots further away from real axis. In these cases, without sufficient refinement, the roots can 'hop away' from their intended branch, landing on and following the branch of another root. In such instances it is typical that conservation of energy is violated and this is a useful signature that increased refinement of the root tracking scheme is needed. Two contrasting examples of the variation of the roots in the complex plane are illustrated in Fig. 2, the first example requiring few steps and the latter many more.

For $\beta_0 \neq 0$, the roots no longer occur in plus/minus pairs and we label the roots $\mu_n^{\pm}$ for $n = 0, 1, 2, \ldots$ to coincide with $\pm\mu_n$ when $\beta_0 = 0$. Typically $\mu_0^{\pm}$ remain on the real axis and any root off the real axis will be paired with a complex conjugate.

We have to be careful to monitor any cases where roots coalesce to form double roots. In fact this will only happen when $D > h$ (a case we will not actually consider in this part of the paper) and the two real roots can coalesce before moving off the real axes as β_0 increases past a critical value. This loss of real roots is associated with total internal reflection for oblique wave incidence into deeper water.

We assume hereafter that $\mu_n^{\pm}$, $n = 0, 1, 2, \ldots$ are known for a prescribed value of β_0 and continue with the solution method. Thus, in $|x| < b$ we now write

$$\varphi(x,z) = \sum_{n=0}^{\infty} c_n \mathrm{e}^{\mathrm{i}\mu_n^+(x+b)} Z_n^+(z) + d_n \mathrm{e}^{\mathrm{i}\mu_n^-(x-b)} Z_n^-(z) \tag{23}$$

where $Z_n^{\pm}(z)$ are defined by (18) with $\mu = \mu_n^{\pm}$. The spatial offset in the exponentials in (23) anticipates the sign of the imaginary part of of $\mu_n^{\pm}$ in such a way that the exponential functions do not exceed a value of unity in magnitude.

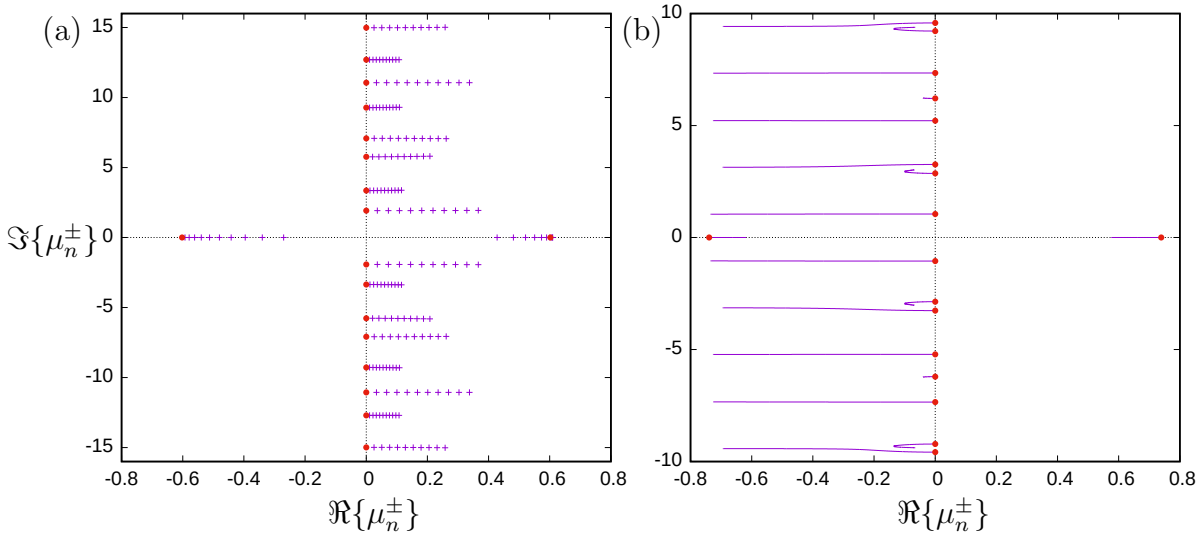

Figure 2: Location of 18 roots $\mu_n^{\pm}$ of the dispersion relation (21) closest to the real axis as β_0 increases from 0° (red circles): (a) in steps of 10° to 90° for $kh = 1$, $d/h = 0.5$, $\Theta = 0.5$ and $\delta = 45°$; (b) in steps of 0.1° to −60° for $kh = 2$, $d/h = 0.25$, $\Theta = 0.9$, $\delta = 30°$.

We now consider the conditions which apply across the two interfaces $x = \pm b$ which will be used to determine the coefficients a_n, b_n in (11) and (12) and c_n and d_n in (23). The methodology applied depends upon the relative size of D and h and the angle of rotation of the plates on the structured bed, δ. We continue by developing a solution method specific to the case $D = h$ and for $\delta \neq 0$. Then

$$\varphi(\pm b^-, z) = \varphi(\pm b^+, z), \qquad \text{for } -h < z < 0 \tag{24}$$

equates pressures through the fluid and matching fluxes gives, after use of the mapping (7) and transformation (10)

$$\varphi_x(-b^-, z) = \begin{cases} \varphi_x(-b^+, z), & -d < z < 0 \\ -(1-\Theta)\sin\delta\Phi_Y|_{x=-b^+}, & -D < z < -d \end{cases} \tag{25}$$

where we note that

$$-(1-\Theta)\sin\delta\Phi_Y|_{x=-b^+} = (1-\Theta)\left(\sin^2\delta\varphi_x(x,-b^+) - \mathrm{i}\beta_0\sin\delta\cos\delta\varphi(x,-b^+)\right). \tag{26}$$

The relation (25) also applies at $x = b$ after replacing $-b^+$ by b^- and $-b^-$ by b^+. Applying (24) to (11) and (23) and using the orthogonality relation (14) gives

$$\mathrm{e}^{-\mathrm{i}\alpha_0 b} + R\mathrm{e}^{\mathrm{i}\alpha_0 b} = \sum_{n=0}^{\infty} c_n(U_{n0}^+ + L_{n0}^+) + d_n\mathrm{e}^{-2\mathrm{i}\mu_n^- b}(U_{n0}^- + L_{n0}^-) \tag{27}$$

and

$$a_m = \sum_{n=0}^{\infty} c_n(U_{nm}^+ + L_{nm}^+) + d_n\mathrm{e}^{-2\mathrm{i}\mu_n^- b}(U_{nm}^- + L_{nm}^-) \tag{28}$$

for $m = 1, 2, \ldots$. Here we have written

$$U_{nm}^{\pm} = \frac{1}{h}\int_{-d}^{0} Z_n^{\pm}(z)\psi_m(z)\,dz \qquad \text{and} \qquad L_{nm}^{\pm} = \frac{1}{h}\int_{-h}^{-d} Z_n^{\pm}(z)\psi_m(z)\,dz \tag{29}$$

which can be calculated explicitly from the definitions of $Z_n^{\pm}(z)$ and $\psi_m(z)$ – see Appendix B. Applying (24) to (12) and (23) at $x = b$ gives

$$T\mathrm{e}^{\mathrm{i}\alpha_0 b} = \sum_{n=0}^{\infty} c_n \mathrm{e}^{2\mathrm{i}\mu_n^+ b}(U_{n0}^+ + L_{n0}^+) + d_n(U_{n0}^- + L_{n0}^-) \tag{30}$$

$$b_m = \sum_{n=0}^{\infty} c_n(U_{nm}^+ + L_{nm}^+)\mathrm{e}^{2\mathrm{i}\mu_n^+ b} + d_n(U_{nm}^- + L_{nm}^-). \tag{31}$$

Application of the condition (25) similarly result in

$$\alpha_0(\mathrm{e}^{-\mathrm{i}\alpha_0 b} - R\mathrm{e}^{\mathrm{i}\alpha_0 b}) = \sum_{n=0}^{\infty} \mu_n^+ c_n(U_{n0}^+ + p_n^+ L_{n0}^+) + \mu_n^- d_n \mathrm{e}^{-2\mathrm{i}\mu_n^- b}(U_{n0}^- + p_n^- L_{n0}^-) \tag{32}$$

and

$$\alpha_m a_m = \mathrm{i}\sum_{n=0}^{\infty} \mu_n^+ c_n(U_{nm}^+ + p_n^+ L_{nm}^+) + \mu_n^- d_n \mathrm{e}^{-2\mathrm{i}\mu_n^- b}(U_{nm}^- + p_n^- L_{nm}^-) \tag{33}$$

where we have written

$$p_n^{\pm} = (1 - \Theta)[\sin^2\delta - (\beta_0/\mu_n^{\pm})\sin\delta\cos\delta]. \tag{34}$$

Finally from applying (25) at $x = b$ we have

$$\alpha_0 T\mathrm{e}^{\mathrm{i}\alpha_0 b} = \sum_{n=0}^{\infty} \mu_n^+ c_n \mathrm{e}^{2\mathrm{i}\mu_n^+ b}(U_{n0}^+ + p_n^+ L_{n0}^+) + \mu_n^- d_n(U_{n0}^- + p_n^- L_{n0}^-) \tag{35}$$

and

$$-\alpha_m b_m = \mathrm{i}\sum_{n=0}^{\infty} \mu_n^+ c_n \mathrm{e}^{2\mathrm{i}\mu_n^+ b}(U_{nm}^+ + p_n^+ L_{nm}^+) + \mu_n^- d_n(U_{nm}^- + p_n^- L_{nm}^-). \tag{36}$$

It is clear we can eliminate R, T, a_m and b_m from between equations (27)–(36). If the infinite series are truncated at $n = N$, and we retain equations from $m = 1, 2, \ldots, N$ then we will have $2N + 2$ equations for the $2N + 2$ unknown constants c_n, d_n, $n = 0, 1, 2, \ldots, N$. After inverting these equations we can recover R, T and a_m, b_m for $m = 1, 2, \ldots, N$ from the equations above.

It is notable that we have not considered the case $D \neq h$ here. It is possible to apply the mode matching method described above to $D < h$, although it complicates the algebra and does not provide much additional insight. The difficulty of solving problems in the more interesting case of $D > h$ is that standard approaches (for equivalent problems involving non-porous steps and trenches see, for example, Evans & McIver (1984), Mei & Black (1969) or Kirby & Dalrymple (1983)) rely upon orthogonal eigenfunctions existing in both $|x| > b$ and $|x| < b$. In our case this presents two problems. The first is that, apart from special cases of $\beta_0 = 0$, or $\delta = 0, \pi/2$, the eigenfunctions $Z_n^{\pm}(z)$ are not orthogonal. It is possible to define a set of eigenfunctions from an adjoint problem in which β_0 is replaced by $-\beta_0$ which satisfy a generalised orthogonality condition when used in conjunction with $Z_n^{\pm}(z)$. However this fails to address a second issue which is that the solution is complicated by the definition of (26). For the reasons above we have postponed consideration of the case $D \neq h$ for general δ, but will consider $D \neq h$ in the special case $\delta = 0$ below.

3 The case $\delta = 0$

When $\delta = 0$, the barriers within $|x| < b$ are aligned with the y-direction and consequently there is no flux across the boundaries $x = \pm b$ for $-h < z < -d$. Thus, while (25) still holds, (24) now only holds for $-d < z < 0$ across the top of the ridge, and the solution outlined in the previous section cannot be applied directly to this special case.

Using $\delta = 0$ (21) is reduced to

$$(1 - \Theta)\beta_0 \tanh[\beta_0(D - d)] = \lambda \frac{K - \lambda \tanh \lambda d}{\lambda - K \tanh \lambda d}. \tag{37}$$

In this case, it can be shown (see Appendix A) in a similar manner to Porter *et al.* (2021) that the only values of λ satisfying (37) lie on the real and imaginary axes. Specifically the values of λ satisfying (37) are $\pm\lambda_0$ on the real axis and $\pm\lambda_n$, $n = 1, 2, \ldots$ lying on the imaginary axis. On account of the relationship (20), the corresponding values of $\mu = \pm\mu_n$ are defined by $\mu_n = \sqrt{\lambda_n^2 - \beta_0^2}$. Consequently μ_n lie on the positive imaginary axis whilst μ_0 lies on the positive real axis for $\lambda_0 > \beta_0$ and μ_0 lies on the positive imaginary axis if $\lambda_0 < \beta_0$. Such a case will only occur when $D > h$ and is associated with total internal reflection as oblique waves pass from shallower water into deeper water.

It is important to note that the depth eigenfunctions $Z_n(z)$ corresponding to the values of μ_n are orthogonal over the interval $-d < z < 0$ and (strangely, perhaps) not the whole range of values of z over which they are defined. To show this we start with the fact that μ_n are distinct and $Z_n(z)$ are real. Then

$$\begin{aligned}(\mu_n^2 - \mu_m^2) \int_{-d}^{0} Z_n(z) Z_m(z)\, dz &= \int_{-d}^{0} Z_n''(z) Z_m(z) - Z_n(z) Z_m''(z)\, dz \\ &= [Z_n'(z) Z_m(z) - Z_n(z) Z_m'(z)]_{-d}^{0} = 0 \end{aligned} \tag{38}$$

after using the governing equation $Z''(z) - (\mu^2 + \beta_0^2)Z(z) = 0$ for $Z(z)$ in $-d < z < 0$, the boundary condition $Z'(0) - KZ(0)$ and the conditions matching $Z_n(z)$, $Z_n'(z)$ at $z = -d$ to the definition of $Z_n(z)$ in $-D < z < -d$ which involves hyperbolic functions whose argument is independent of n. Thus, it must be that

$$\frac{1}{d} \int_{-d}^{0} Z_n(z) Z_m(z)\, dz = C_n \delta_{nm} \tag{39}$$

where C_n can easily be calculated from the definition of $Z_n(z)$ in $-d < z < 0$ given by (18) with $\mu = \mu_n$; it is defined in Appendix B.

Unlike the general problem with plates rotated through a non-zero angle, once $\delta = 0$ the geometry is symmetric about the vertical plane $x = 0$. The solution is made simpler by decomposing the potential into the sum of even and odd parts via

$$\phi(x, y, z) = \frac{1}{2}(\phi^s(x, y, z) + \phi^a(x, y, z)) \tag{40}$$

such that

$$\phi^s(x, y, z) = \phi^s(-x, y, z), \qquad \phi^a(x, y, z) = -\phi^a(-x, y, z). \tag{41}$$

Consequently the problems for $\phi^{s,a}$ need only be solved in $x < 0$ when supplemented with the conditions

$$\frac{\partial \phi^s}{\partial x} = \phi^a = 0, \qquad \text{on } x = 0. \tag{42}$$

Additionally, if we write

$$\phi^{s,a}(x,y,z) \sim (\mathrm{e}^{\mathrm{i}\alpha_0 x} + R^{s,a}\mathrm{e}^{-\mathrm{i}\alpha_0 x})\mathrm{e}^{\mathrm{i}\beta_0 y}\psi_0(z), \qquad \text{as } x \to -\infty \tag{43}$$

then it follows from (4) and (40) with (41) that

$$R = \frac{1}{2}(R^s + R^a), \qquad T = \frac{1}{2}(R^s - R^a). \tag{44}$$

We are now in a position to write down general expansions for the potentials in $x < -b$ and $-b < x < 0$. We first factorise the y dependence inherited from the incident wave with

$$\phi^{s,a}(x,y,z) = \varphi^{s,a}(x,z)\mathrm{e}^{\mathrm{i}\beta_0 y} \tag{45}$$

and then

$$\varphi^{s,a}(x,z) = (\mathrm{e}^{\mathrm{i}\alpha_0 x} + R^{s,a}\mathrm{e}^{-\mathrm{i}\alpha_0 x})\psi_0(z) + \sum_{n=1}^{\infty} a_n^{s,a}\mathrm{e}^{\alpha_n(x+b)}\psi_n(z) \tag{46}$$

in $x < -b$ where α_n have been defined after (12). In $-b < x < 0$ we have

$$\varphi^s(x,z) = \sum_{n=0}^{\infty} c_n^s \frac{\cos\mu_n x}{\cos\mu_n b} Z_n(z) \qquad \text{and} \qquad \varphi^s(x,z) = \sum_{n=0}^{\infty} c_n^a \frac{\sin\mu_n x}{\sin\mu_n b} Z_n(z) \tag{47}$$

satisfying (42) where $c_n^{s,a}$ are coefficients to be determined and the factors in the denominator normalise the functions of x.

The matching conditions at the common interface are that $\varphi^{s,a}(x,z)$ is continuous across $x = -b$ and that

$$\varphi_x^{s,a}(-b^-,z) = \begin{cases} \varphi_x^{s,a}(-b^+,z) & -d < z < 0 \\ 0, & -h < z < -d. \end{cases} \tag{48}$$

Note that we have no information relating to $\varphi^{s,a}(-b^+,z)$ or $\varphi_x^{s,a}(-b^+,z)$ for $-D < z < -d$ as the boundary $x = -b^+$ is absorbed by the homogenisation within the microstructure. We could follow the previous method and use the orthogonality of eigenfunctions in $x < -b$ to determine systems for equations for coefficients from the matching conditions, following the approach of Evans & McIver (1984) for example. Instead, we follow the methods advocated by Mei & Black (1969), Porter & Evans (1995) and formulate integral equations for functions relating to the unknown horizontal velocity above the edge of the ridge at $x = -b$ for which the establishment of the orthogonality condition (39) is vital.

We let $U^{s,a}(z) = \varphi_x^{s,a}(-b^-,z) = \varphi_x^{s,a}(-b^+,z)$ over $-d < z < 0$. Combining this definition with (46) we get

$$\mathrm{i}\alpha_0 h(\mathrm{e}^{-\mathrm{i}\alpha_0 b} - R^{s,a}\mathrm{e}^{\mathrm{i}\alpha_0 b}) = \int_{-d}^{0} U^{s,a}(z)\psi_0(z)\,dz \tag{49}$$

and

$$\alpha_n h a_n^{s,a} = \int_{-d}^{0} U^{s,a}(z)\psi_n(z)\,dz \tag{50}$$

using (14). Using the expansions (47) and the orthogonality condition (39) we find that

$$\mu_n d c_n^s \tan\mu_n b = \frac{1}{C_n}\int_{-d}^{0} U^s(z)Z_n(z)\,dz, \qquad \mu_n d c_n^a \cot\mu_n b = \frac{1}{C_n}\int_{-d}^{0} U^a(z)Z_n(z)\,dz, \tag{51}$$

for $n = 0, 1, 2, \ldots$. Matching (46) to (47) over $x = -b$, $-d < z < 0$ and using the relations (50) and (51) to eliminate all unknowns (apart from $R^{s,a}$) we arrive at

$$\int_{-d}^{0} U^{s,a}(z')K^{s,a}(z,z')\,dz' = -(\mathrm{e}^{-\mathrm{i}\alpha_0 b} + R^{s,a}\mathrm{e}^{\mathrm{i}\alpha_0 b})\psi_0(z), \qquad -d < z < 0 \tag{52}$$

where

$$K^s(z,z') = \sum_{n=1}^{\infty} \frac{\psi_n(z)\psi_n(z')}{\alpha_n h} - \sum_{n=0}^{\infty} \frac{Z_n(z)Z_n(z')}{C_n \mu_n d \tan \mu_n b} \tag{53}$$

and $K^a(z,z')$ is defined as above but with $\tan \mu_n b$ replaced by $-\cot \mu_n b$. We proceed by letting

$$U^{s,a}(z) = -(\mathrm{e}^{-\mathrm{i}\alpha_0 b} + R^{s,a}\mathrm{e}^{\mathrm{i}\alpha_0 b})u^{s,a}(z) \tag{54}$$

such that $u^{s,a}(z)$ is the only unknown satisfying the integral equation

$$\int_{-d}^{0} u^{s,a}(z')K^{s,a}(z,z')\,dz' = \psi_0(z), \qquad -d < z < 0. \tag{55}$$

Introducing the definition (54) into (49) gives

$$\mathrm{i}\alpha_0 h(\mathrm{e}^{-\mathrm{i}\alpha_0 b} - R^{s,a}\mathrm{e}^{\mathrm{i}\alpha_0 b}) = -(\mathrm{e}^{-\mathrm{i}\alpha_0 b} + R^{s,a}\mathrm{e}^{\mathrm{i}\alpha_0 b}) \int_{-d}^{0} u^{s,a}(z)\psi_0(z)\,dz \tag{56}$$

and so it follows that

$$R^{s,a} = \mathrm{e}^{-2\mathrm{i}\alpha_0 b}\left(\frac{\alpha_0 h - \mathrm{i}A^{s,a}}{\alpha_0 h + \mathrm{i}A^{s,a}}\right) \tag{57}$$

where

$$A^{s,a} = \int_{-d}^{0} u^{s,a}(z)\psi_0(z)\,dz. \tag{58}$$

Once $R^{s,a}$ is determined, all other coefficients in the problem can also be determined from $u^{s,a}(z)$. Thus we are just left requiring to solve (55) for $u^{s,a}(z)$ which is performed by introducing an approximation in which the unknowns are expanded in a finite series of $P+1$ terms

$$u^{s,a}(z) \approx \sum_{p=0}^{P} w_p^{s,a} u_p(z) \tag{59}$$

and $w_p^{s,a}$ are coefficients weighting the expansion functions $u_p(z)$, $p = 0, \ldots, P$. We are not able to determine the local behaviour of the solution in the vicinity of the corner of the ridge, but have imagined that the flow around the edge at $(x,z) = (-b,-d)$ is similar to that around an isolated thin barrier protruding upwards to this point. This allows us to follow the approximation of Porter & Evans (1995) used exactly for such barrier configurations. In this approach, we first relate $\hat{u}_p(z)$ to $u_p(z)$ by

$$\hat{u}_p(z) = u_p(z) - K\int_{-d}^{z} u_p(\zeta)\,d\zeta \tag{60}$$

such that $\hat{u}_p(z)$ has zero derivative at $z = 0$ since the functions $u_p(z)$ are related to ϕ_x which itself satisfies (2). Also, $u_p(z)$ should incorporate the anticipated inverse square root behaviour of ϕ_x at as z approaches $-d$. Thus we make the choice

$$\hat{u}_p(z) = \frac{2(-1)^p T_{2p}(z/d)}{\pi\sqrt{d^2 - z^2}} \tag{61}$$

	$kh=0.25$, $\theta_0=0^\circ$		$kh=2.5$, $\theta_0=60^\circ$	
N	$\lvert R\rvert$	$\lvert E\rvert$	$\lvert R\rvert$	$\lvert E\rvert$
4	0.162670	10^{-16}	0.139759	8.1×10^{-6}
8	0.162727	10^{-16}	0.139991	1.7×10^{-6}
16	0.162743	10^{-16}	0.140059	3.5×10^{-8}
32	0.162746	10^{-15}	0.140077	2.5×10^{-8}
64	0.162747	10^{-16}	0.140082	2.8×10^{-9}

Table 1: Convergence of $|R|$ and $|E|=|1-|R|^2-|T|^2|$ with truncation parameter, N, for $\Theta=0.1$, $\delta=30^\circ$, $b/h=1$.

where $T_{2p}(z)$ is a Chebychev polynomial, even across $z=0$. The outcome of the implementation of the Galerkin approximation, in which (59) is substituted into (55) before being multiplied by $u_q(z)$ and integrated over $-d<z<0$, is

$$\sum_{p=0}^{P} w_p^{s,a} K_{pq}^{s,a} = G_{q0}, \qquad q=0,1,\ldots,P \tag{62}$$

where

$$K_{p,q}^{s} = \sum_{n=1}^{\infty} \frac{G_{qn}G_{pn}}{\alpha_n h} - \sum_{n=0}^{\infty} \frac{H_{qn}H_{pn}}{C_n \mu_n d \tan \mu_n b} \tag{63}$$

and K^a differs with tan replaced by $-\cot$ whilst

$$G_{pn} = N_n^{-1/2} \cos k_n h J_{2p}(k_n d), \qquad \text{for } n\geq 1 \text{ with} \qquad G_{p0} = (-1)^p N_0^{-1/2} \cosh khI_{2p}(kd), \tag{64}$$

expressed in terms of Bessel and modified Bessel functions. Also, we find

$$H_{pn} = (-1)^p I_{2p}(\mu_n d) \equiv J_{2p}(-\mathrm{i}\mu_n d) \tag{65}$$

recalling that μ_n are imaginary for $n\geq 1$ and possibly imaginary for $n=0$ also. Once $w_p^{s,a}$ are determined from (62) we have from using (59) in (58) and working through the details from Porter & Evans (1995) that

$$A^{s,a} \approx \sum_{p=0}^{P} w_p^{s,a} G_{p0}. \tag{66}$$

One of the advantages of using this method is that it is known from Porter & Evans (1995) to be rapidly convergent and here we will confirm that $P=5$ is normally sufficient for six decimal place accuracy computations of $R^{s,a}$ (indeed often smaller values of P will suffice). We have used expansion functions with an inverse cube root singularity at the edge $(x,z)=(-b,-d)$ (e.g. Evans & Fernyhough (1995)) and confirmed these results converge quickly to the same results as those computed with the choice (61). We can also easily confirm that the system of equations in (62) is real and hence $A^{s,a}$ is real from (66) which then implies from (57) that $|R^{s,a}|=1$ which is required by conservation of energy.

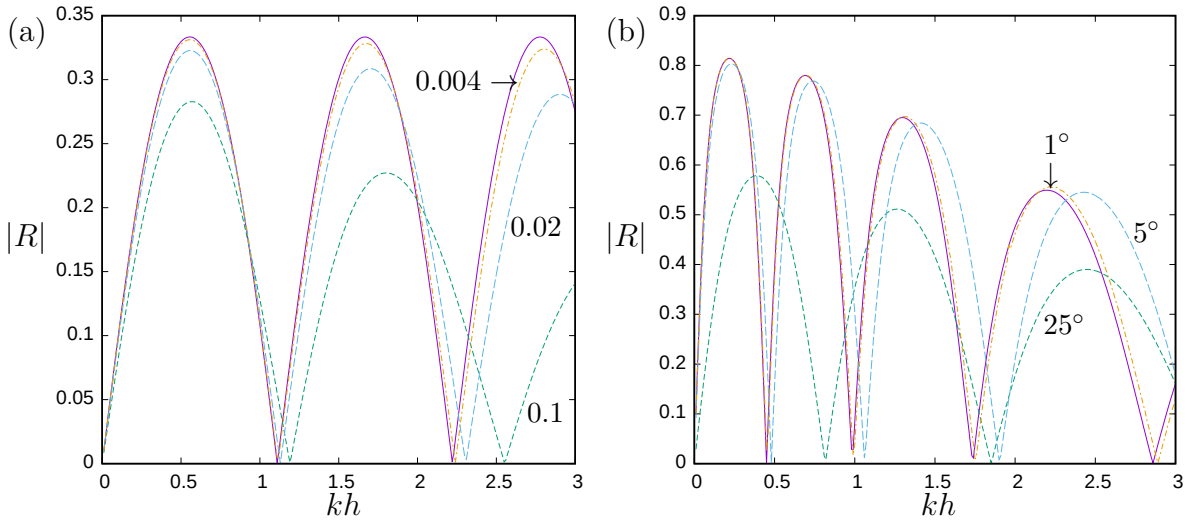

Figure 3: Variation of $|R|$ against kh for $\theta_0 = 0°$, $b/h = 1$ and thin barriers ($\Theta = 0$). In (a) $\delta = 45°$ and curves for $d/h = 0.1,\ 0.02,\ 0.004$ are shown converging to results for full depth barriers (solid/purple). In (b) $d/h = 0.1$ and $\delta = 25°,\ 5°,\ 1°$ are shown converging to results for equivalent rigid step (solid/purple).

4 Results

Before discussing the quantitative behaviour of the results, we state the key finding of this work.

When either θ_0 is replaced by $-\theta_0$, or δ is replaced by $-\delta$, we find that the computed values of $|R|$ and $|T|$ at the same frequency are unchanged, irrespective of other geometric parameters in the problem. This symmetry of the reflection and transmission coefficients in wave heading and the array orientation was the principle highlight of the work of Porter (2021) who considered thin barriers ($\Theta = 0$) extending throughout the depth. It was subsequently also shown to hold under a shallow water approximation to scattering by rectangular structured ridges by Marangos & Porter (2021). In the context of these established results it is perhaps not surprising that the same result holds for the full depth-dependent model of wave scattering. Nevertheless, taken on its own, it is a remarkable result. For instance, since waves are perfectly transmitted *for all frequencies* by thin barriers ($\Theta = 0$) of *any* non-zero rotation δ and *any* submergence depth d/h provided the wave heading is aligned with the barriers ($\theta_0 = \delta - \pi/2$) it follows that waves are also perfectly transmitted for all wave frequencies by the same structure when the wave heading is reversed to $\theta_0 = \pi/2 - \delta$.

The invariance of $|R|$, $|T|$ to changes in sign of either θ_0 or δ can be established from the formulation of the solution presented in §2. It is based on (21) and the observation that if $\mu_n^{\pm}$ are labelled as the eigenvalues corresponding to the parameters (θ_0, δ) then the eigenvalues corresponding to either $(-\theta_0, \delta)$ or $(\theta_0, -\delta)$ are $-\mu_n^{\mp}$. It readily follows that if $Z_n^{\pm}(z)$ are the eigenfunctions for (θ_0, δ) then $Z_n^{\mp}(z)$ are eigenfunctions for the cases $(-\theta_0, \delta)$ or $(\theta_0, -\delta)$. Next, from (23), if $\varphi(x, y)$ is the general solution corresponding to (θ_0, δ) then $\varphi(-x, y)$ becomes the general solution for $(-\theta_0, \delta)$ or $(\theta_0, -\delta)$. This is equivalent to flipping the plate array about $x = 0$, or, equivalently, to sending in incident waves from plus infinity rather than minus infinity. Either way this reduces the problem to one in which either the sign of θ_0 or δ has been reversed.

The main purpose of Fig. 3(a,b) and Fig. 4 is to show how results convergence to various established cases. We continue by illustrating the convergence of the numerical scheme based on

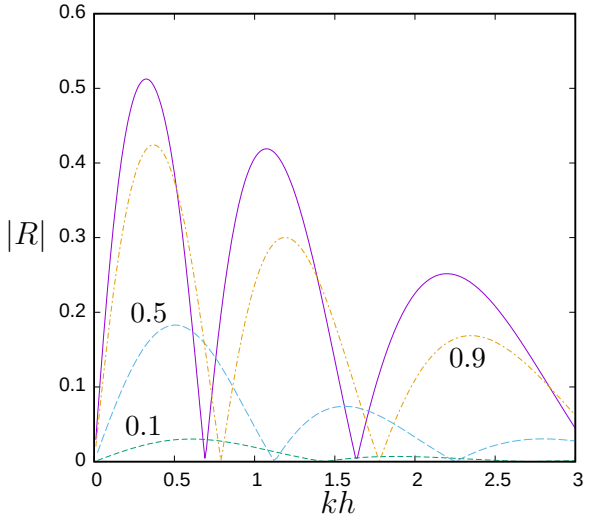

Figure 4: Variation of $|R|$ against kh for $b/h = 1$, $d/h = 0.25$ and $\theta_0 = 30°$, $\delta = -60°$. In (a) $\Theta = 0.1$, 0.5, 0.9 are shown converging to results for equivalent rigid step (solid/purple).

the approach adopted in §2 based on eigenfunction matching through the fluid depth. In addition to the numerical methods required to locate the complex roots of (21), already discussed in §2, we must determine how many roots are required. This is a set by the truncation of the infinite system of equations in §2 to $m, n = 0, 1, \ldots, N$.

Table Tab. 1 provides two contrasting cases of low frequency and high frequency for a ridge occupying a 75% of the water depth. At lower frequencies, fluid velocities decrease less rapidly with the depth than at higher frequencies. It is therefore typical that more depth functions are required to resolve the interaction with the submerged ridge for lower frequencies although this expected feature is not especially clear from the results presented, which illustrate that only a few modes are required for two to three decimal place accuracy. Also shown in Tab. 1 are values of $|E|$ where $E = 1 - |R|^2 + |T|^2$ and conservation of energy demands that $E = 0$. It seems from Tab. 1, and other computations performed in the preparation of this work, that energy conservation is automatically satisfied for normal incidence and is only used as an indicator of convergence for values of $\theta_0 \neq 0$. Numerical convergence can be much slower for more extreme parameter values including $\Theta \to 1$, $d/h \to 0$, $\delta \to 0$. For example, for $\delta = 1°$, $kh = 2.5$, $d/h = 0.1$, $\Theta = 0.9$, $b/h = 1$ we find $|E| = 3.8 \times 10^{-3}$ ($N = 64$), $|E| = 2.2 \times 10^{-3}$ ($N = 128$).

Thus, in Fig. 3(a) we have examined the effect of reducing d/h in the case $\Theta = 0$ and comparing with the Porter's (2021) explicit results for $|R|$ for thin barriers extending through the depth. In Fig. 3(b) we the effect that rotating the barriers towards being aligned perpendicular to the normally-incident waves has on an arrangement of thin barriers extending to $d/h = 0.1$. In this case, we confirm that $|R|$ tends to results for a rigid impermeable step, computed using methods devised for Evans *et al.* (2015), applying Porter's (1995) integral equation method to the general approach described in Mei & Black (1969). This is expected, since for normal incidence on closely-spaced arrays of plates, there will be no fluid motion in the narrow gaps between the plates.

In Fig. 4 we compare again with results from a rigid step, but choose to increase Θ from 0 (thin barriers) towards 1 where the gaps close up completely. Numerically it is hard to go further than $\Theta = 0.9$, but the trend is clear. In this arrangement, the barriers are aligned with the wave heading and in the case $\Theta = 0$ it follows (confirmed numerically) that $|R| = 0$ for all kh. On account of the symmetry in $|R|$ to reversal in the signs of θ_0 or δ the same curves shown in Fig. 4

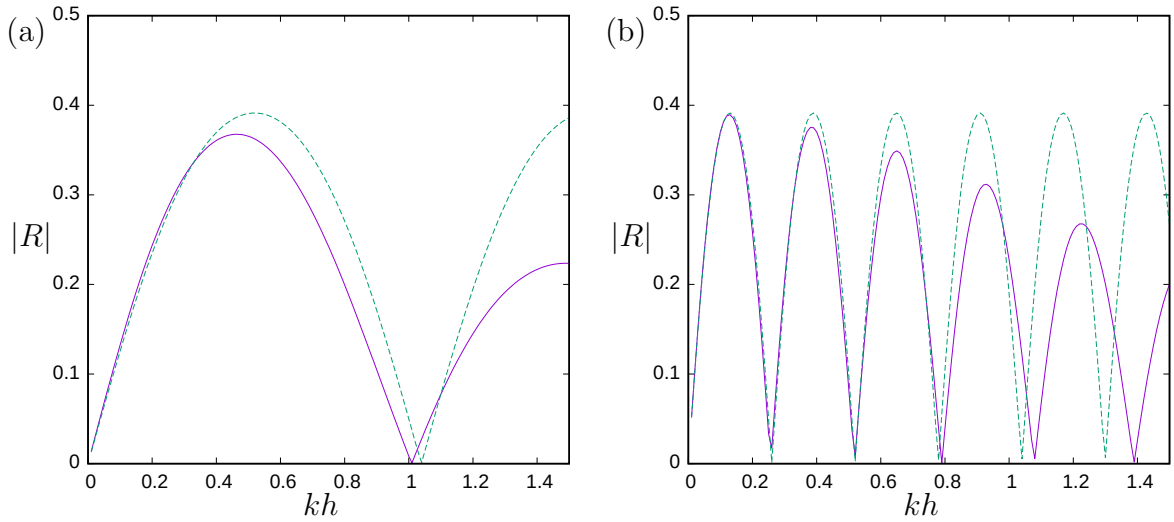

Figure 5: Variation of $|R|$ against kh for $d/h = 0.25$ and $\theta_0 = 0°$, $\delta = 45°$, $\Theta = 0.5$ and (a) $b/h = 1$, (b) $b/h = 4$: full depth-dependent theory (solid/purple), shallow water approximation (green/dashed).

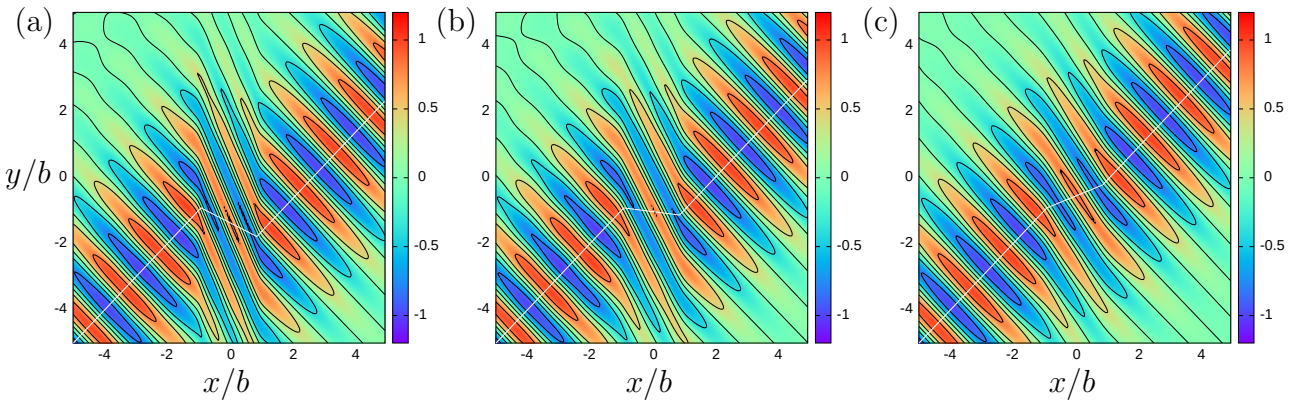

Figure 6: The instantaneous surface when a Gaussian beam centred on $\theta_0 = 45°$ is incident on a structured ridge of width $b/h = 2$, $\delta = 45°$, $\Theta = 0$ with: (a) $d/h = 0.1$; (b) $d/h = 0.2$; (c) $d/h = 0.4$.

are produced when $\theta_0 = -30°$, $\delta = -60°$ or when $\theta_0 = 30°$, $\delta = 60°$.

We make comparisons with the shallow water (long wavelength) approximation of Marangos & Porter (2021) in Fig. 4 which confirms that results are in good agreement for $kh \ll 1$. It also shows the effect of varying the width of the ridge whose main influence is determining multiple interference effects due to reflection of waves propagating across the ridge at their edges, $x = \pm b$.

Next, we illustrate the refractive characteristics of the structured bed. In Fig. 6 three plots are shown of the instantaneous free surface for an incident Gaussian beam from $x = -\infty$ centred around $\theta_0 = \theta_c = 45°$ in the case of $\delta = 45°$, $\Theta = 0$ so that the thin barriers forming the plate array are perpendicular to the central wave heading. At the central heading, $\theta_0 = 45°$, there is perfect transmission on account of the symmetry of the reflection coefficient in θ_0. However, we expect small amounts of wave reflection from the contributions to from wave angles around θ_0 which have

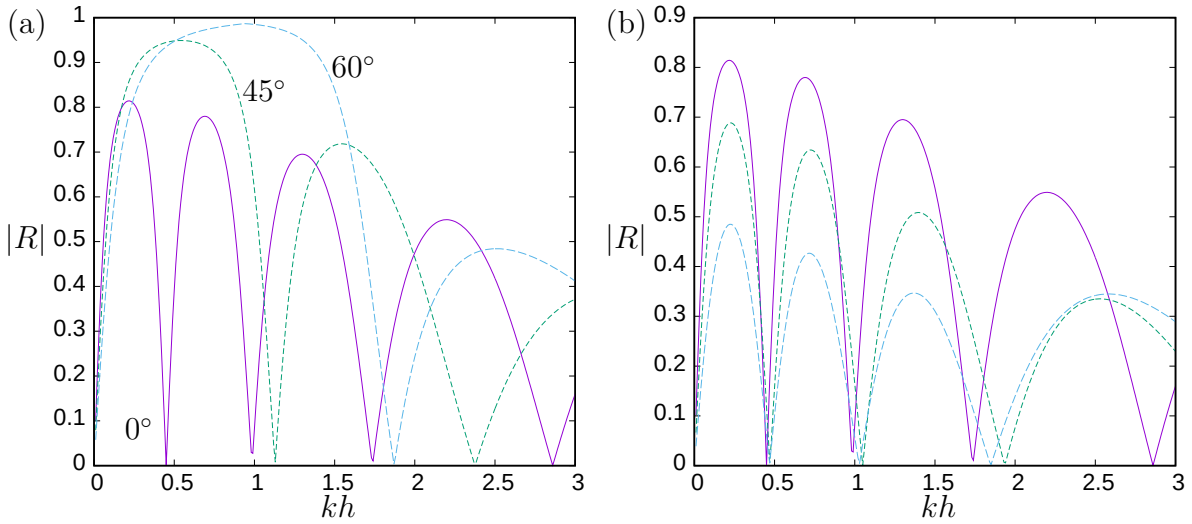

Figure 7: Variation of $|R|$ against kh for $d/h = 0.1$, $\delta = 0°$, $\Theta = 0$, $b/h = 1$ with (a) $D/h = 2$ and (b) $D/h = 0.2$: $\theta_0 = 0°$ (purple/solid), $\theta_0 = 45°$ (green/dashed), $\theta_0 = 60°$ (light blue/long dashed).

been subject to a Gaussian weighting. That is, in Fig. 6 we have plotted

$$\phi_{beam}(x, y; \theta_c) = 2\sqrt{\pi} \int_{\theta_c - \Delta\theta}^{\theta_c + \Delta\theta} \cos(\theta_0 - \theta_c) \mathrm{e}^{-4\pi^2(\theta_0 - \theta_c)^2} \phi(x, y; \theta_0)\, d\theta_0 \tag{67}$$

where, for numerical purposes, $\Delta\theta$ truncates the range of values over which the integration is performed (we used $\Delta\theta = 30°$). The three subplots in Fig. 6 show the influence of the depth of submergence of the barriers in the array for a fixed width, $b/h = 2$, and wavenumber, $kh = 2$. When the barriers extend through 90% of the depth ($d/h = 0.1$) the waves are negatively refracted by the ridge and resemble figures shown in Porter (2021) for barriers extending fully through the depth. White lines are overlaid on the plots to indicate the path of the centre of the Gaussian beam. As the ridge height decreases the refractive effect of the ridge weakens and when $d/h = 0.4$ (Fig. 6(c)) we observe that the refraction is conventional (positive).

4.1 The case $\delta = 0$

The special case of $\delta = 0$ is computed using values of $P = 5$ in (62) and truncation of the infinite summation in (63) to 500 terms. This determines $|R|$ and $|T|$ to six decimal place accuracy in all cases under investigation. The roots λ_n of (37) are found numerically following the description given in Appendix A, all lying on either the real or imaginary axes.

When $\theta_0 = 0$, the fluid in the narrow gaps between the plates does not move and values of $|R|$ coincide with those for a rigid step submerged to a depth d, irrespective of the depth of the fluid in the gaps, D. This can be seen in Fig. 7(a,b) in which the curves for $\theta_0 = 0°$ are identical to the solid curve in Fig. 2(b). In Fig. 7 we have concentrated on the effect the internal fluid depth, D, a new parameter which we can only adjust in this special $\delta = 0$ case. Thus, we have plotted the variation of $|R|$ for $D/h = 2$ and $D/h = 0.2$ in Figs. 7(a) and (b) in the case that $d/h = 0.1$ for two oblique incident wave headings of 45° and 60°. Whilst there is no difference for $\theta_0 = 0°$, we can see that the internal fluid depth has a significant effect on reflection for oblique wave angles. When

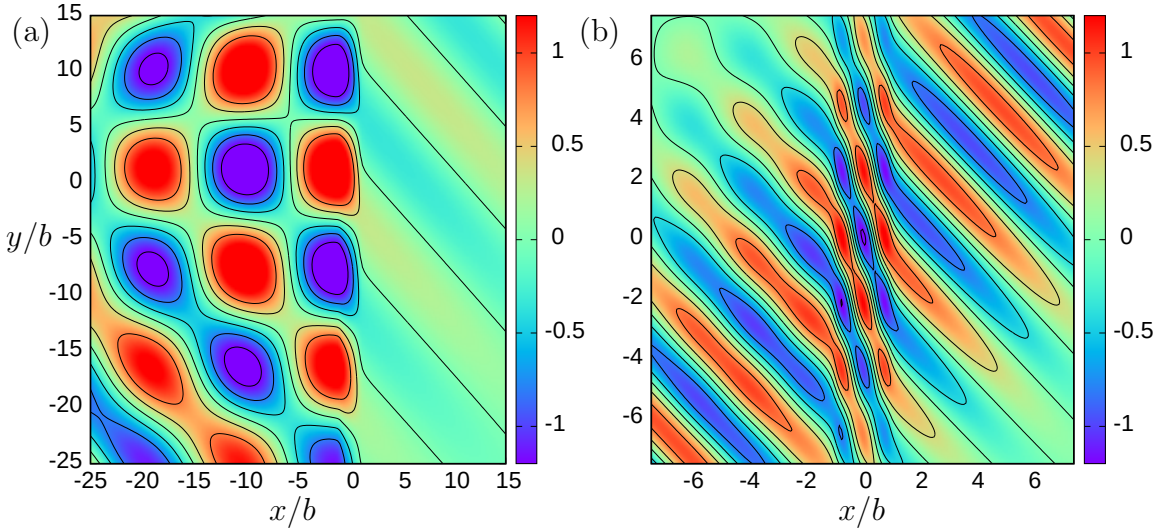

Figure 8: The instantaneous surface when a Gaussian beam centred on $\theta_0 = 45°$ is incident on a structured ridge of width $b/h = 1$, $\delta = 0°$, $d/h = 0.1$, $\Theta = 0$ with: (a) $kh = 0.5$, $D/h = 2$; (b) $kh = 2$, $D/h = 0.2$.

$D/h > 1$ the reflection increases for longer wavelengths whilst reduced internal depths, $(D/h < 1)$ results in a decrease reflected energy as θ_0 increases.

We have used Gaussian beams centred around $\theta_0 = 45°$ to showcase the reflective qualities of the ridge with the large internal fluid depth $D/h = 2$ at $kh = 0.5$ in Fig. 8(a). There is much higher reflected energy from this structured device at these oblique incident angles over a wide range of frequencies than for the equivalent rigid step or thin barrier. In contrast, Fig. 8(b) relates to $D/h = 0.2$ and $kh = 2$ where there is much more typical transmission over the step with normal (positive) refraction into the shallower fluid depths.

5 Conclusions

In this paper, we have shown how full depth-dependent linear theory has been applied to solve a scattering problem involving a long submerged horizontal ridge of closely-spaced plate arrays. The effect of the local structure of a discrete plate array has been modelled using a approximate effective medium equation which has previously been confirmed as a good approximation to a discrete array. Two mathematical solution approaches have been developed depending on the parameters in the problem. When the plates are not aligned with the direction of the ridge we have used an eigenfunction matching method to determine the reflection and transmission of oblique incident waves. The mathematical challenge here has been in determining the complex eigenvalues of the dispersion relation. On account of the solution method employed for general plate array orientations only the case when the fluid depth within the array matches that outside the array has been considered. When the plates are aligned with the ridge, the boundary conditions at the ends of the ridge change character and a special solution is required which does allow the internal fluid depth to differ from that outside the array. This case has been approached by developing integral equations for functions relating to the horizontal velocity across the top corner of the ridge and solving via a Galerkin method.

The range of configurations described by the theory in the paper allow us to demonstrate a

number of cases in which numerical results which can be validated against existing results. One of the purposes of this paper has been to confirm that the simpler shallow water model of wave propagation of Marangos & Porter (2021) is a good approximation to the full depth dependent models for sufficiently small values of kh (roughly $kh \lesssim \frac{1}{2}$). A key result is to show that the perfect transmission predicted by Porter (2021) for plate arrays with thin barrier elements extending at incident wave angles opposite to the array orientation angle is also a feature of barriers extending partially through the depth. In doing so, we have demonstrated that submerged plate arrays are capable to producing negative refraction the effect being stronger for longer waves and for barriers closer to the surface.

For plate arrays aligned with the ridge, we have shown that the reflection of sufficiently long obliquely incident waves over a structured ridge with an internal fluid depth exceeding the fluid depth away from the ridge is enhanced when compared with an equivalent impermeable ridge or a vertical barrier submerged to the same depth. This may be of interest to the design of offshore breakwater systems.

Acknowledgement

RP acknowledges support from the EPSRC grant number EP/V04740X/1. CM has been supported by an EPSRC Studentship number S139151-124.

A Roots of the dispersion relation for $\delta = 0$

In this Appendix we discuss the roots of the dispersion relation given by (37), in relation to the special case $\delta = 0$ which we write in the form

$$\mathcal{C} = R(\lambda) \equiv \lambda \frac{K - \lambda \tanh \lambda d}{\lambda - K \tanh \lambda d} \tag{68}$$

and

$$\mathcal{C} = (1 - \Theta)\beta_0 \tanh[\beta_0(D - d)] \tag{69}$$

is a real and non-negative constant. The following arguments are very similar to Porter *et al.* (2021).

The case of $\beta_0 = 0$ is trivial, since (68) is reduced to finding roots of $K = \lambda \tanh \lambda d$ which coincides with the water wave dispersion relation for a fluid depth d. This (e.g. Linton & McIver (2001)) is known to result in a pair of real roots and an infinite sequence of roots lying symmetrically on the imaginary axis.

When λ is assumed real and positive different cases arise, depending on the sign of $1 - Kd$ the value of $R(0) \equiv R_0 = K/(1 - Kd)$. If $Kd > 1$ then $R_0 < 0$, and there is an asymptote of $R(\lambda)$ at $\lambda = \lambda^*$ where $\lambda^* = K \tanh \lambda^* d$. Away from this asymptote $R(\lambda)$ is a monotonically decreasing function which crosses the axis at a value of $\lambda^\dagger > \lambda^*$ corresponding to the positive real root of $K = \lambda^\dagger \tanh \lambda^\dagger d$ and continues as $R(\lambda) \sim -\lambda$ as $\lambda \to \infty$. Therefore there is a single root λ_0 of (68) satisfying $\lambda^* < \lambda_0 < \lambda^\dagger$. Since $R(\lambda)$ is an even function, there is a corresponding negative root, $-\lambda_0$.

If $Kd < 1$ there are no zeros of the denominator of $R(\lambda)$ which is monotonic decreasing function from a positive value of R_0 at $\lambda = 0$, crossing the axis at $\lambda^\dagger$ and with $R(\lambda) \sim -\lambda$ as $\lambda \to \infty$. Thus there are real roots $\pm\lambda_0$ only if $\mathcal{C} < R_0$. These two scenarios are illustrated in Fig. 9

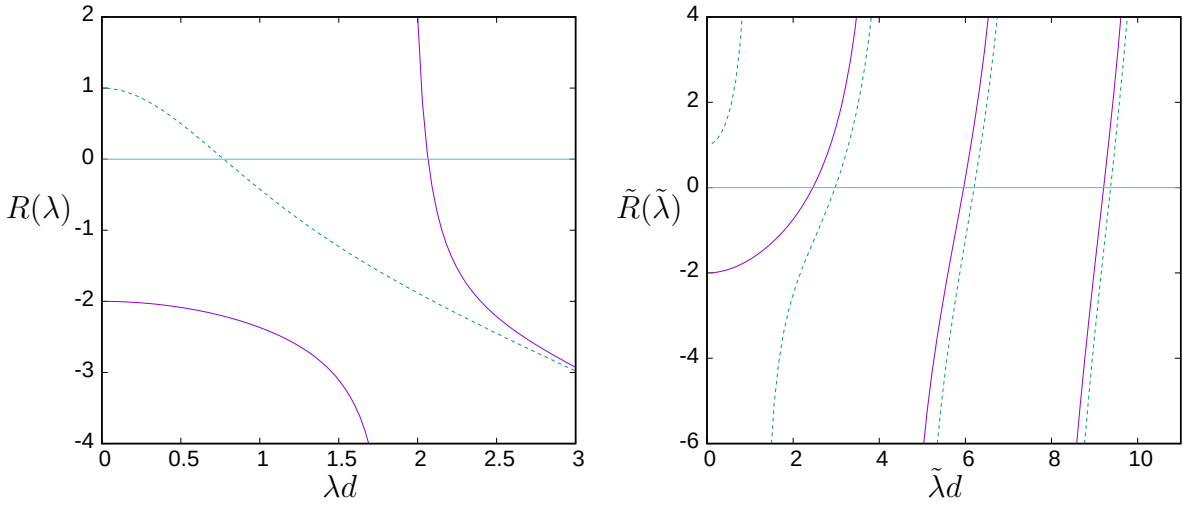

Figure 9: A graphical illustration of variation of functions relating to the real and imaginary roots of the dispersion relation: purple (solid) curve, $Kd = 2$; green (dashed) curve, $Kd = \frac{1}{2}$.

Now consider $\lambda = \mathrm{i}\tilde{\lambda}$ where $\tilde{\lambda}$ is assumed real and positive whereby (68) is transformed into

$$\mathcal{C} = \tilde{R}(\tilde{\lambda}) \equiv \tilde{F}_1(\tilde{\lambda})/\tilde{F}_2(\tilde{\lambda}) \tag{70}$$

where

$$\tilde{F}_1(\tilde{\lambda}) = \tilde{\lambda}\sin\tilde{\lambda}d + K\cos\tilde{\lambda}d, \qquad \tilde{F}_2(\tilde{\lambda}) = \cos\tilde{\lambda}d - (K/\tilde{\lambda})\sin\tilde{\lambda}d. \tag{71}$$

We again have two consider different cases depending on the sign of $Kd - 1$. When $Kd > 1$ the asymptotes of the right-hand side of (70) lie at zeros of $\tilde{F}_2(\tilde{\lambda})$ located in intervals $n\pi < \tilde{\lambda}d < (n+\frac{1}{2})\pi$ for $n = 1, 2, \ldots$. In between asymptotes $\tilde{R}(\tilde{\lambda})$ is monotonic increasing and passes through zeros of $\tilde{F}_1(\tilde{\lambda})$ at roots of the water wave dispersion relation for a fluid of depth d, located between $(n - \frac{1}{2})\pi < \tilde{\lambda}d < n\pi$. Thus we can infer there is an infinite sequence of roots, $\pm\lambda_n$ $(n = 1, 2, \ldots)$ of (68), lying on the imaginary axes between each of these zeros and the asymptote that follows each zero.

When $Kd < 1$ the first asymptote at $\tilde{\lambda} = \tilde{\lambda}^*$ of $\tilde{F}_2(\tilde{\lambda})$ lies between zero and $\pi/2$. For values of $\tilde{\lambda} > \tilde{\lambda}^*$ beyond this asymptote, $\tilde{R}(\tilde{\lambda})$ increases monotonically and all the arguments of the previous paragraph apply. For $0 < \tilde{\lambda} < \tilde{\lambda}^*$, $\tilde{R}$ remains monotonic increasing from $\tilde{R}(0) = R_0$. In other words, there is an additional root in $0 < \tilde{\lambda} < \tilde{\lambda}^*$ if $Kd < 1$ and $\mathcal{C} > R_0$ which we label λ_0 since it only exists when the real root ceases to exist. That is to say, λ_0 is the same root and either lives on the real or imaginary axis depending on certain conditions being met. A graphical illustration of this information is provided in Fig. 9.

Finally, we can use Rouché's theorem (e.g. Ablowitz & Fokas (1997, p.263)) to show that there are no roots lying in the complex plane off the real or imaginary axes. Again the arguments follow quite closely the details described in Porter *et al.* (2021). We write (68) as

$$F(\lambda) = F_1(\lambda) + F_2(\lambda) = 0$$

where

$$F_1(\lambda) = K\cosh\lambda d - \lambda\sinh\lambda d, \qquad F_2(\lambda) = \mathcal{C}((K/\lambda)\sinh\lambda d - \cosh\lambda d).$$

Then F_1 and F_2 are meromorphic functions and Rouché's theorem states that the number of zeros of $F = F_1 + F_2$ inside a closed contour C in the complex plane is equal to the number of zeros of F_1 provided $|F_1| > |F_2|$ for all points on C.

We consider the rectangular contour $C = C_m(\rho)$ comprised of four straight-line segments. Two are defined by $\Im\{\lambda\} = \pm p_m$, $-\rho < \Re\{\lambda\} < \rho$ where p_m is the mth positive zero of $(K/p_m)\sin p_m d - \cos p_m d = 0$. The other two segments complete the rectangle by setting $\Re\{\lambda\} = \pm\rho$ and letting $-p_m < \Im\{\lambda\} < p_m$. Then it can be shown that $|F_1| > |F_2|$ on each $C_m(\rho)$ with $\rho \to \infty$. The zeros of F_1 are just those for the water wave dispersion relation which are known to be located on the real and imaginary axes at locations previously described. When we count the number of zeros of F that we have identified as being located on the real and imaginary axes inside the contour $C_m(\rho)$ with $\rho \to \infty$, we find they are the same as the number of zeros of F_1. Therefore, by Rouché's theorem, and taking the limit $m \to \infty$, we conclude that there are no zeros of F other than those on the real and imaginary axes.

B Definition of depth integrals

From the definition of (29) we find, after extensive algebra in which the dispersion relation for k and (21) are both used, that

$$U^{\pm}_{nm} = \frac{-N_m^{-1/2}A(\mu)}{(\lambda^2 + k_m^2)h}\left(k_m \sin k_m(h-d)\cosh\kappa(h-d) + \kappa(1-\Theta)\cos k_m(h-d)\sinh\kappa(h-d)\right) \quad (72)$$

where $\lambda^2 = \mu^2 + \beta_0^2$, $\kappa = \mu\sin\delta - \beta_0\cos\delta$, $A(\mu)$ is defined by (19) and $\mu = \mu_n^{\pm}$. For $m = 0$ when $k_0 = -\mathrm{i}k$,

$$U^{\pm}_{n0} = \frac{N_0^{-1/2}A(\mu)}{(\lambda^2 - k^2)h}\left(k\sinh k(h-d)\cosh\kappa(h-d) - \kappa(1-\Theta)\cosh k(h-d)\sinh\kappa(h-d)\right). \quad (73)$$

It is slightly less complicated to determine that

$$L^{\pm}_{nm} = \frac{N_m^{-1/2}A(\mu)}{(k_m^2 + \kappa^2)h}\left(k_m \sin k_m(h-d)\cosh\kappa(h-d) + \kappa\cos k_m(h-d)\sinh\kappa(h-d)\right) \quad (74)$$

such that

$$L^{\pm}_{n0} = \frac{N_0^{-1/2}A(\mu)}{(k^2 - \kappa^2)h}\left(k\sinh k(h-d)\cosh\kappa(h-d) - \kappa\cosh k(h-d)\sinh\kappa(h-d)\right). \quad (75)$$

When $\lambda = k$ and/or $\kappa = k$, (73) and/or (75) need revising either by recalculating integrals from the start or by taking limits of the expressions given.

The value of C_n defined by (39) is evaluated as

$$C_n = \frac{1}{2}(1 - (K/\lambda_n)^2) + (1 + (K/\lambda_n)^2)\frac{\sinh 2\lambda_n d}{4\lambda_n d} - \frac{K\sinh^2\lambda_n d}{\lambda_n^2 d} \quad (76)$$

with $\lambda_n^2 = \mu_n^2 + \beta_0^2$ determined by (37).

References

[1] Ablowitz, MJ., Fokas, AS. 1997. Complex variables: introduction and applications. Cambridge University Press.

[2] Berraquero, CP., Maurel, A., Petitjeans, P. Pagneux, V. 2013. Experimental realization of a water-wave metamaterial shifter. Phys. Rev. E. **88**, 051002.

[3] Chen, H., Yang, J., Zi, J., Chan, CT. 2009. Transformation media for linear liquid surface waves. EuroPhys. Lett. **85**, 24004.

[4] Evans, DV., Fernyhough, M. 1995. Edge waves along periodic coastlines. Part 2. J. Fluid Mech. **297**, 307–325.

[5] Evans, DV., McIver, P. 1984. Edge waves over a shelf: full linear theory J. Fluid Mech. **142**, 79–95.

[6] Evans, DV., McIver, M., Porter, R. 2015. Transparency of structures in water waves. Proc. Int. Workshop on Water Waves and Floating Bodies, Osaka, Japan.

[7] Farhat, M., Enoch, S., Guenneau, S., Movchan, A. 2008. Broadband cylindrical acoustic cloak for linear surface waves in a fluid. Phys. Rev. Lett. **101**, 134501.

[8] Farhat, M., Guenneau, S., Enoch, S., Movchan, A. 2010. All-angle-negative-refraction and ultra-refraction for liquid surface waves in 2D phononic crystals. J. Comp. Appl. Math. **234**(6), 2011–2019.

[9] Hu, X., Yang, J., Zi, J., Chan, CT. Ho, K-M. 2013. Experimental observation of negative effective gravity in water waves. Sci. Rep. **3**, 1916.

[10] Kirby, JT., Dalrymple, RA. 1983. Propagation of obliquely incident water waves over a trench J. Fluid Mech. **133**, 47–63.

[11] Linton, CM., McIver, P. 2001. Handbook of mathematical techniques for wave/structure interactions. Chapman Hall/CRC Press.

[12] Maier, SA. (Ed) 2018. World Scientific Handbook Of Metamaterials And Plasmonics (In 4 Volumes). World Scientific: Singapore.

[13] Marangos, C., Porter, R. 2021. Shallow water theory for structured bathymetry. Proc. Roy. Soc. A., **477**: 20210421.

[14] Maurel, A., Marigo, J-J., Cobelli, P, Petitjeans, P., Pagneux, V. 2017. Revisiting the anisotropy of metamaterials for water waves. Phys. Rev. B. **96**, 134310.

[15] Maurel, A., Pham, K., Marigo, J-J. 2019. Scattering of gravity waves by a periodically structured ridge of finite extent. J. Fluid Mech. **871**, 350–365.

[16] Mei, CC., Black, JL. 1969. Scattering of surface waves by rectangular obstacles in waters of finite depth. J. Fluid Mech. **38**, 499–511.

[17] Porter, R. 2021. Plate arrays as water wave metamaterials. Wave Motion **100**, 102673.

[18] Porter, R., Evans, DV. 1995. Complementary approximations to wave scattering by vertical barriers. J. Fluid Mech. **294**, 155–180.

[19] Porter, R., Zheng, S., Liang, H. 2021 Scattering of surface waves by truncated structured cylinders. Submitted for publication.

[20] Zareei, A., Alam, M-R. 2015. Cloaking in shallow-water waves via nonlinear medium transformation. J. Fluid Mech. **778**, 273–287.

[21] Zheng, S., Porter, R., Greaves, D. 2020. Wave scattering by an array of metamaterial cylinders. J. Fluid Mech. **903**, A50.